RSC Advances

PAPER

View Article Online
View Journal | View Issue



Cite this: *RSC Adv.*, 2025, **15**, 44584

# Synthesis and characterization of a modified diatomite-based hybrid shell microcapsule for thermal energy storage

Meng Zhou, Songyang Liu, Weinan Wang and Guangshan Zhu *

In this paper, modified diatomite (MDE) was used for the moisture adjustment substrate, and lauryl-cetyl alcohol (LAL–CAL) was utilized as the phase change material (PCM) to synthesize MDE-based hybrid shell microcapsule PCMs (MDE-MPCMs) with humidity and temperature control functions through the sol–gel method. Fourier transform infrared spectroscopy was used to study the chemical compatibility between MDE and LAL–CAL. The effects of different MDE content for humidity regulation, heat storage, and surface temperature response behaviors of MDE-MPCMs were studied through humidity regulation experiments, differential scanning calorimetry, and infrared thermal imaging technology. The results showed that LAL–CAL was successfully coated within the hybrid shell structure, and the moisture absorption capacity and thermal stability of MPCM were enhanced after the introduction of MDE. When MDE content was 15%, the moisture absorption rate of MDE-MPCM3 reached 16.63%, and the corresponding latent heat value was 70.01 J $g^{-1}$. Those results demonstrated that MDE-MPCM3 exhibited superior moisture regulation performance and thermal storage capacity, which can effectively mitigate environmental temperature and humidity fluctuations. Therefore, the novel MDE-MPCM3 has considerable potential in energy storage and improving environmental comfort.

Received 12th October 2025
Accepted 9th November 2025

DOI: 10.1039/d5ra07802d

rsc.li/rsc-advances



## 1 Introduction

Temperature and relative humidity (RH) are important indices to assess the comfort of the indoor environment, and are also closely related to the durability and energy consumption of constructions.[1–4] For a long time, many mechanical control facilities, such as HVAC, heaters, and humidifiers, have become the main force for measuring temperature and humidity, resulting in a large amount of building energy consumption and greenhouse gas emissions.[5–7] The passive regulation method can automatically sense the change of surroundings, thus endowing the functions of building structures with temperature and humidity regulation, and achieving energy conservation by relying on the characteristics of the building enclosure systems. At present, much attention has been drawn to porous mineral materials with moisture absorption properties and PCMs with thermal management capability in the application of passive energy-saving buildings.[8,9] However, most of the existing studies have focused on heat storage performances[10–12] or humidity management behaviors.[13–15] How to combine hygroscopic porous mineral materials with PCMs efficiently to prepare the composite materials with temperature and humidity adjustment functions has become an important research focus.[16]

*School of Green Mining and Resource Engineering, Liaoning Petrochemical University, Fushun 113001, China. E-mail: zgslnsh@163.com*

According to the different thermal energy storage mediums, there are three forms of sensible heat storage, chemical heat storage, and latent heat storage (phase change heat storage).[17,18] Compared with the other two types of heat storage, latent heat storage has a higher energy storage density and near-constant temperature during the heat storage and release process, and can effectively narrow the imbalance between energy supply and demand, which is widely used in intelligent temperature controlling, solar energy utilization, and building energy conservation.[19–22] As an important latent heat storage medium, PCMs can absorb and release heat during the phase change process, thus displaying excellent temperature regulation performance.[23–25] It can be divided into two types according to chemical properties, organic and inorganic PCMs.[26] Organic PCMs (fatty acids,[27] fatty alcohols,[28] *etc.*) with low cost, corrosion resistance, better phase change performance, and higher latent heat of melting compared with inorganic PCMs, which have a larger potential for wide application in the field of solar energy utilization and building energy conservation. However, the phase change temperature of single PCM was difficult to meet the requirements of temperature control in energy-saving buildings, while eutectic PCMs can adjust the temperature to the appropriate range.[29] Significantly, the liquid phase leakage issue immensely constrains the application of eutectic PCMs in energy-efficient buildings and must be encapsulated before use. Microencapsulation is a prominent measure to seal up the PCM by covering its droplets with a successive film and limiting the

PCM in a certain space.[30] Inorganic shell materials have the merits of high thermal conductivity, excellent thermal stability, and strong flame retardant compared to organic shells, and are often a better choice for shell materials, such as $SiO_2$,[31,32] and $TiO_2$.[33] However, inorganic shell materials possess stronger adhesion with the matrix, and it is easy to form a loose crumb structure, which may cause the precipitation of core materials during mixing with building materials. To improve the compactness of shell materials, it is necessary to synthesize the hybrid shell microcapsules. Yuan *et al.* prepared double-layer organic phase change microcapsules with *n*-eicosane and poly-dopamine/poly (melamine-formaldehyde) as the core and shell material.[34] The DSC results found that the energy storage density can be reached optimum when the content of *n*-eicosane is 85%, which has the phase change enthalpy (199.4 J $g^{-1}$) while ensuring thermal stability.

Humidity control materials (HCMs) can absorb and release moisture from the air, and restrain indoor humidity fluctuations without consuming energy, which has become the research focus in building energy conservation and improving the living environment.[35] Some porous mineral materials (zeolite,[36] sepiolite,[37] *etc*.) are widely used in building envelopes due to the larger specific surface area and suitable pore structure, which can realize the adsorption and release of water vapor to achieve the regulation of RH.[38] DE is characterized by widespread, lower cost, non-toxicity, stronger absorption capacity, and higher chemical stability, and is a natural HCM composed of amorphous silica.[39–42] Fort *et al.* prepared a novel gypsum board by adding stable DE-based composite PCM and superabsorbent polymer.[43] The results showed that the hygroscopic properties of gypsum were improved, and the moisture buffer capacity was increased to 2.38 g/(%$RHm^2$). Mao *et al.* designed the DE-based hygroscopic coating materials with a metal–organic framework by adding MIL-100(Fe) to the composite scallop shell powder-based and DE-based HCMs mixed with 20 wt% zeolite.[44] The results indicated that the moisture adsorption amount and rate for DE were 0.0201 g $g^{-1}$ and 4.62 g $m^{-2}$ $h^{-1}$, which were 3 and 3.88 times that of pure DE, respectively. Hu *et al.* prepared three kinds of composite HCMs at the calcination temperatures of 650, 750, and 900 °C by using DE and ground calcium carbonate as raw materials.[45] It was indicated that the 72 h moisture adsorbed amount of DG750 was 0.46, 0.54, and 0.53 times of DE at 98%, 85%, and 75% RH, respectively. However, the pores of raw DE are usually blocked by organic matter and debris impurities, which will reduce the porosity, water transfer efficiency, and thermal energy storage space. Li *et al.* used the microwave-acid leaching method to modify DE and add expanded graphite (EG) to improve the latent heat capacity and thermal conductivity.[46] The results show that the thermal conductivity of the sample with EG is 3.2 times that of the pure sample, and the loading of the PCM is 72.2%. Zhang *et al.* used acid treatment, high-speed shearing, and ultrasonic waves to optimize the microstructure of DE, which not only improved the silica content but also changed the porosity.[47]

HCMs and PCMs can respectively regulate indoor humidity and temperature and are widely used in improving circumstantial comfort. By combining HCMs and PCMs effectively, temperature and humidity control can be achieved at the same time. In recent years, mineral-based HCMs and PCMs have been used to prepare dual-function materials with temperature and humidity regulation, which has become a hot topic in energy-saving.[48,49] Yang *et al.* prepared a kind of composite phase change humidity control wallboard with expanded perlite, paraffin, and diatom mud, and characterized hygrothermal performance.[50] The results indicated that the wallboard can effectively adjust the indoor temperature and humidity. Wang *et al.* synthesized the functional material for temperature and humidity regulation with sepiolite and zeolite as HCMs and capric acid as PCMs.[37] The results showed that the sepiolite-zeolite powder doped with capric acid phase change microcapsules can keep the RH at 51.75–58.84%, and reduce the temperature fluctuation by 2 and 3 °C. Yang *et al.* developed a new type of DE-based gypsum board that controlled temperature and humidity simultaneously.[51] It was evidenced that compared with ordinary gypsum board, DE-based gypsum board demonstrates satisfactory performance in terms of heat storage and temperature delay. It is feasible to prepare the composite material with temperature and humidity adjustment functions, which were applied to improve energy utilization rates by combining mineral-based HCMs with PCMs. At present, most scholars focus on the heat storage properties of phase change microcapsules. However, few studies on constructing hybrid shell microcapsules with humidity and temperature regulation by mineral-based HCMs secondary encapsulation PCMs, and the synergistic mechanism of moisture and heat transfer need to be explored.

In this study, the MDE-MPCMs with temperature and humidity regulation functions were designed by using MDE as the matrix material and LAL–CAL as the core material. The pore structure of DE and MDE was studied by physical adsorption experiments. The surface morphology, thermostability, and phase transition performance of the samples were systematically investigated. It was worth noting that the influence of 5–20% MDE content on the hygrothermal properties of MDE-MPCMs was comprehensively studied, and the synergistic mechanism of moisture and heat regulation was systematically discussed. Additionally, the economics of MDE-MPCM3 were further analyzed. As the natural mineral, DE incurs a cost of approximately 120 USD per ton, LAL amounts to 3300 USD per ton, and CAL reaches 2100 USD per ton. Generally, the price of the porous support composite PCMs was prepared by using *n*-octadecane as an organic PCM, which is nearly 5 00 000 USD per ton. This novel MDE-MPCMs presents a more cost-effective alternative to the application of current composite PCMs, providing substantial benefits for applications in thermal energy storage and humidity control material.

## 2 Experimental

### 2.1 Materials

The DE came from Linjiang Yuantong's new material company, and the main chemical composition was $SiO_2$, $Al_2O_3$, and $Fe_2O_3$. LAL ($C_{12}H_{26}O$) was purchased from Teco Brown Chemical Co.,

Ltd, and CAL ($C_{16}H_{34}O$) was provided by Sinopharm Chemical Reagent Co., Ltd Sodium dodecyl sulfate (SDS, AR, Sinopharm Chemical Reagent Co., Ltd) was mixed with LAL–CAL as a surfactant to prepare the emulsion. Tetraethyl orthosilicate (TEOS, 99% pure, Huangshan City Jiahua Silicone Technology Co., Ltd) was employed to produce shell material for sealing LAL–CAL. The other materials involved in the reaction process were hydrochloric acid (HCl, adjust the pH value, Shenzhen Jinyi Trading Co., Ltd), anhydrous ethanol, and deionized water (DIW, which was laboratory tap water), all of which are analytical grade and can be applied directly without further purification. NaOH purchased from Kehua test reagent consumables, used to modify DE.

## 2.2 Experimental procedure

**2.2.1 DE performance optimization.** DE was modified by first calcining and then using the alkali dissolution method before use. First, take 100 g of DE into the crucible, and put it in the muffle furnace for calcination. The effects of calcination temperature and time on the moisture absorption and release rate of DE were considered by the humidity control experiment, and the results showed that the optimum process was 400 °C per 3 h. Then, the calcined DE was treated with alkali under the optimum technology, and the influence of the liquid–solid ratio (the mass ratio of NaOH solution to DE, L/S) for the humidifying ability of MDE was tested by employing NaOH solution with a concentration of 5%. It was found that the L/S was 6 : 1, and DE has the best moisture absorption rate. The sample was prepared according to the optimum condition and named MDE.

**2.2.2 Preparation of LAL–CAL eutectic mixture.** Before preparing the LAL–CAL, it was necessary to predict the proportion of mixtures according to the second law of thermodynamics and the MATLAB model. The phase transition temperature and latent heat of LAL and CAL were obtained by DSC test, respectively, and then the content of each component in the LAL–CAL phase transition system was determined according to the calculation formula.[52] Solving the equation gives that the theoretical mass ratio of the lowest eutectic point of LAL–CAL was 85 : 15. According to the mass ratio, weigh LAL and CAL into the beaker and mix. Heat the beaker in a constant water bath temperature of 80 °C and stir for 30 min to ensure even mixing. Eventually, the beaker was cooled and solidified at room temperature, and the obtained sample was sealed for later use.

**2.2.3 Synthesis of MDE-MPCMs.** Based on the sol–gel method, MDE was self-assembled in LAL–CAL emulsion, and a series of moisture-heat controlled microcapsule materials containing MDE hybrid shells were prepared by adjusting the pH value of the system to initiate the polymerization of $SiO_2$ solution and emulsion. Fig. 1 shows the fabrication schematic diagram of MDE-MPCMs. First, 1.5 g MDE and 0.1 g SDS were added to 20 mL DIW and stirred for 10 min to obtain the well-dispersed MDE. Second, 10 g LAL–CAL and 0.8 g SDS were added to 100 g DIW and bathed at 60 °C for 1 h to obtain a stable oil–water emulsion. Third, 10 g TEOS and 10 mL anhydrous ethanol were added to 20 mL DIW, and the pH value of the solution was adjusted to 2 and 3 through drop-wise addition of HCl solution with a concentration of 0.1 mol $L^{-1}$ until a colorless and transparent $SiO_2$ solution was obtained by hydrolysis under the water bath at 60 °C for 30 min. Subsequently, the well-dispersed MDE was added into the stable LAL–CAL emulsion, mixed evenly, and a drop-wise addition of $SiO_2$ solution to prepare the hybrid shell microcapsule emulsion with a water bath at 60 °C for 3 h. Ultimately, the emulsion was aged for 24 h. The hybrid shell microcapsule emulsion was filtered after the end of the reaction, which was washed with DIW, and dried at 40 °C for 24 h to obtain the solid sample, and named MDE-

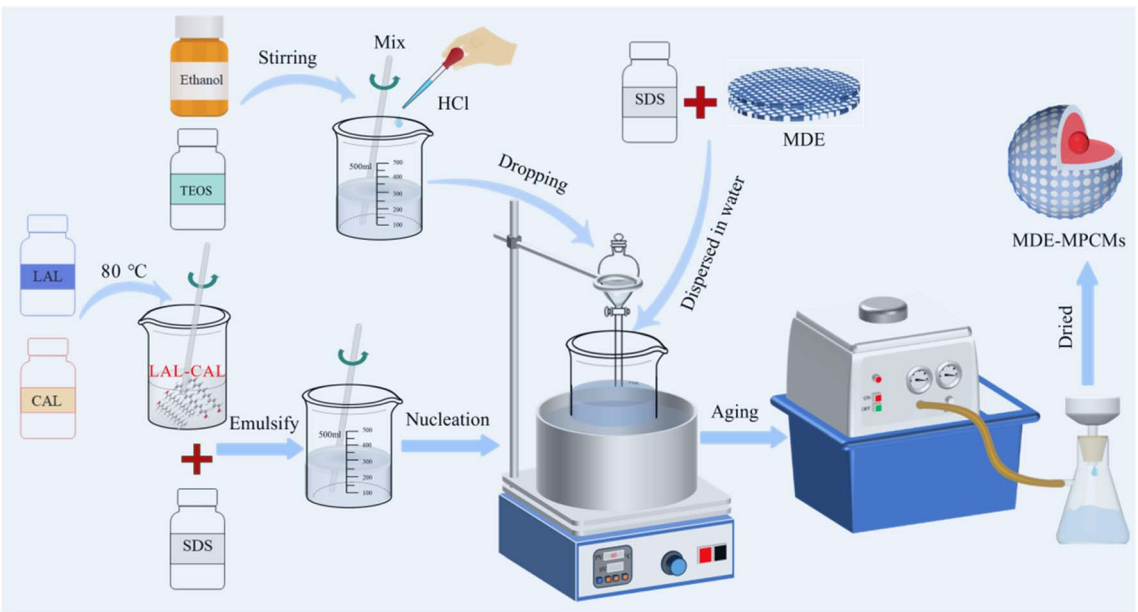


Fig. 1 Schematic illustration of the preparation process for MDE-MPCMs.

MPCM3 (MDE content 15%). Only the amount of MDE was changed, while the other components were unchanged. The remaining samples were prepared by adding 5%, 10%, and 20% MDE content under the same conditions and named MDE-MPCM1, MDE-MPCM2, and MDE-MPCM4, respectively.

### 2.3 Characterization

The pore structure type and specific surface area of DE and MDE were determined by Autosorb-IQ2-MP, and the surface hydrophilicity was measured by the physics instruments OCA15EC contact angle meter. The crystal structure of the samples was measured by X-ray diffractometer (XRD, Bruker D8 Advance) with the range from 5° to 80° at a constant rate of 5° per min. Fourier transformation infrared spectroscopy (FTIR, Bruker TENSOR27) was used to analyze the chemical compatibility of the materials at a resolution of 4 $cm^{-1}$ in the range of 4000–400 $cm^{-1}$. Following GB/T20312-2006, the humidity control characteristics of the sample were studied under constant temperature and humidity conditions. First, the weighing bottle was washed and dried, and then weighed after cooling, recorded as $M_0$. Afterward, the samples were taken into the weighing bottles, transferred to the drying oven to remove moisture content, and weighed as $M_1$. Finally, the weighing bottle with samples was placed in the dryer containing a saturated salt solution, and the mass was weighed at intervals, denoted as $M_i$. The hygroscopic process was maintained at 20 °C and 100% RH for 48 h, and then immediately allowed to release moisture at 11% RH for 48 h. The electronic balance was used for all weighing (accuracy 0.1 mg), and the moisture absorption and release rate of samples were calculated. The thermal regulation performance of the MDE-MPCMs was measured by the infrared thermal imager A700. The phase transformation process and thermal performances of PCMs and MDE-MPCMs were examined by differential scanning calorimetry (DSC, Q20) under nitrogen conditions, in which the temperature scanning range was 0–100 °C and the rate was 5 °C $min^{-1}$. Instrument accuracy: temperature 0.01 °C, enthalpy value 0.05%. To evaluate the thermal cycling stability of MDE-MPCM3, the 50 and 100 repetitions of phase transition cycling experiments were conducted in the same test tubes and named as MDE-MPCM3-50 and MDE-MPCM3-100, respectively. The test tubes were first placed in the low-temperature chamber (16 °C) in order to reach a stable frozen state of the samples, and then moved to a constant-temperature water bath (50 °C). The thermogravimetric analyzer (TGA, Q600, Instrument accuracy 0.1%) was used to evaluate the thermal stability of MDE, LAL–CAL, and MDE-MPCM3 under the nitrogen atmosphere from room temperature to 600 °C, and the heating rate was 10 °C $min^{-1}$. The leakage experiment tests the morphological stability of samples. LAL–CAL and MDE-MPCM3 were pressed into sheets and then heated to 50 °C, during which changes in surface temperature were observed once in 30 s. The morphology and microstructure of DE, MDE, and MDE-MPCM3 were characterized by FEI Quanta-200 scanning electron microscopy (SEM).

## 3 Results and discussion

### 3.1 Pore structure characteristics

A larger specific surface area and reasonable pore size distribution can enhance the adsorption capacity of MDE and improve the moisture and heat transfer performance. Fig. 2 reveals the $N_2$ adsorption–desorption and pore size distribution curve of DE and MDE. In Fig. 2a, when the relative pressure was lower ($P/P_0$ < 0.1), the adsorption capacity of DE was small, indicating that the number of micropores was fewer. With the growth of relative pressure, $N_2$ adsorption also increased rapidly, and $H_3$ hysteretic rings appeared in the relative pressure between 0.4 and 0.9, evidencing that there are a lot of mesoporous structures in DE. Based on IPUAC, the adsorption–desorption curve of DE belongs to a type IV isotherm. The BET model shows that the specific surface area of MDE increased from 16.72 to 22.13 $m^2 g^{-1}$, and the BJH method indicates that

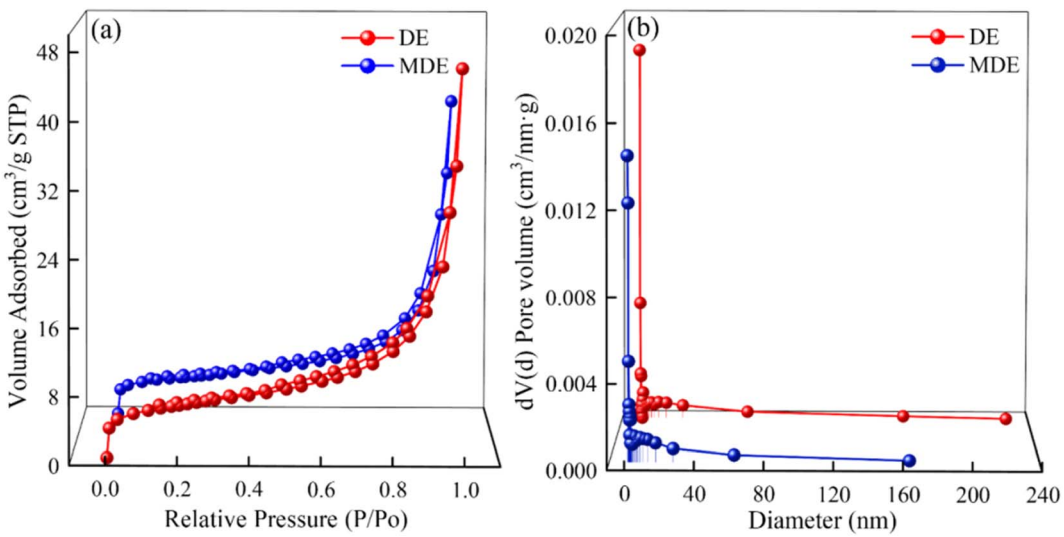


Fig. 2 (a) The $N_2$ adsorption–desorption isotherm and (b) BJH pore size distribution curve of DE and MDE.

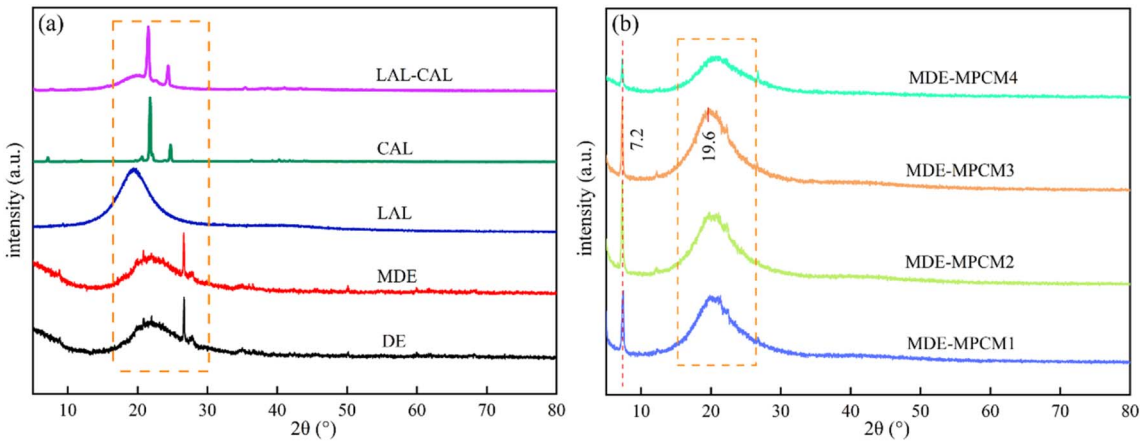


Fig. 3 XRD patterns of (a) DE, MDE, and PCMs, (b) MDE-MPCMs.

the pore volume expanded from the original 0.069 to 0.080 $cm^3 g^{-1}$. The BJH pore size distribution curve of DE as shown in Fig. 2b, and it can be known that the mesoporous distribution of DE was mainly in the range of 2–40 nm. Compared with DE, the number of macropores in MDE was reduced, and the pore size distribution was more reasonable, showing a trend of fine and dense. The larger specific surface area and abundant mesoporous structure endowed MDE with excellent adsorption properties, which is beneficial to increase the heat storage space and promote water transfer.

### 3.2 Crystal structure analysis

The crystal structures of DE, MDE, PCMs, and MDE-MPCMs were analyzed by XRD test technology. In Fig. 3a, DE presented a typical amorphous structure, and several strong peaks appeared in the range from 18° to 30°, which were diffraction peaks of amorphous $SiO_2$. MDE did not have obvious characteristic peak strength change, the crystal structure also did not change, and it was still dominated by amorphous $SiO_2$. For PCMs, the diffraction patterns of LAL showed a prominent peak in the range of about $2\theta = 18–25°$, CAL shows sharp diffraction at $2\theta = 21°$ and 25°, which the diffraction peaks correspond to one-to-one in LAL–CAL, and the positions were the same. It means that the crystal structures of LAL and CAL did not disappear during the recombination process, which was a simple physical interaction. Fig. 3b shows XRD patterns of MDE-MPCMs. The sharp crystal diffraction appeared at 7.2°, which was the diffraction peak of the silica wall material prepared by the sol–gel method. Amorphous diffraction occurred at 18–25°, close to the position of the MDE and LAL–CAL diffraction peaks, indicating that LAL–CAL was successfully coated by MDE-based hybrid shell material. With the increase of MDE content from 5% to 20%, the diffraction peak intensity of MDE-MPCMs presented the trend of first increasing and then decreasing, which indicated that there was weak physical interaction and no chemical reaction during the secondary packaging of LAL–CAL in MDE.

### 3.3 Chemical compatibility determination

Fig. 4 displays the FTIR spectra of DE, MDE, PCMs, and MDE-MPCMs. As shown in Fig. 4a, DE and MDE had five prominent absorption peaks, which were the O–H vibration

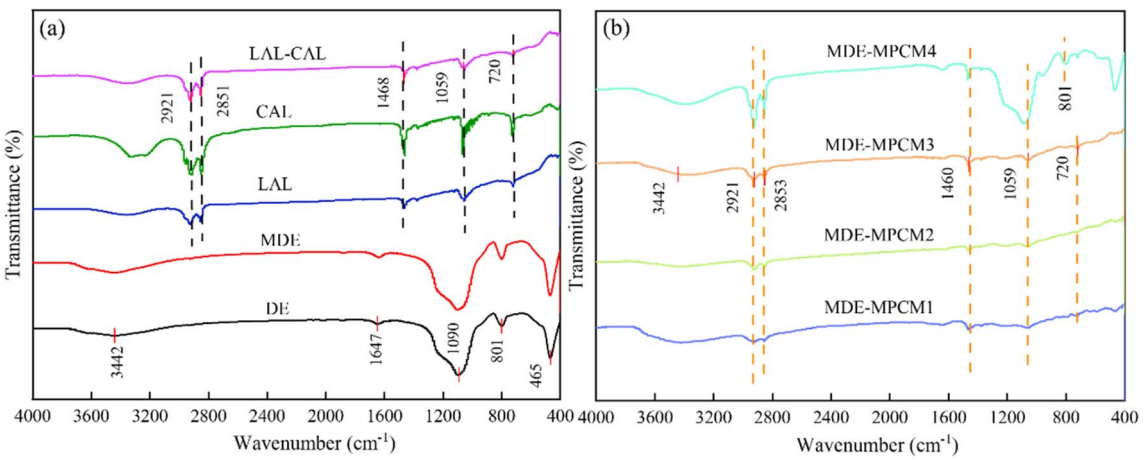


Fig. 4 The FTIR spectra of (a) DE, MDE, and $PCM_S$, (b) MDE-MPCMs.

stretching peak near 3442 and 1647 $cm^{-1}$, and the strong absorption peak at 1090 $cm^{-1}$ was the Si–O asymmetric stretching vibration, the Si–O–Si symmetric vibration near 801 $cm^{-1}$, and the bending vibration peak generated at 465 $cm^{-1}$. Fully indicates that amorphous $SiO_2$ was the main component of DE and MDE. For the FTIR spectra of PCMs, the absorption peaks of LAL and CAL at 3360 $cm^{-1}$ were the contraction vibration peak of the O–H group, and the peak near 2921 and 2851 $cm^{-1}$ was caused by the antisymmetric vibration of C–H and the symmetric vibration of $-CH_2$. At 1468, 1059, and 720 $cm^{-1}$, there are strong and weak absorption peaks caused by C–H bending vibration, C–O stretching vibration, and C–OH swaying vibration, respectively. The absorption peaks of LAL and CAL can be found in the spectra of the binary eutectic, which further demonstrates that there was no chemical reaction between them. The FTIR spectra of MDE-MPCM1, MDE-MPCM2, MDE-MPCM3, and MDE-MPCM4 as shown in Fig. 4b. The corresponding characteristic peaks of MDE and LAL–CAL appeared near 3442, 2921, 2853, 1460, 1059, and 720 $cm^{-1}$, and the strength depends on the proportion of each single amount in MDE-MPCMs. It was worth noting that the absorption peaks of microcapsules at 1059 and 720 $cm^{-1}$ were unchanged significantly when the content of MDE was 5–15%. However, the diffraction peak of MDE appears obviously in the MDE-MPCM4 at 1059 and 801 $cm^{-1}$ when the content reaches 20%, which may be that excessive MDE will affect the formation of microcapsules. The absorption peaks of MDE and LAL–CAL were successfully found in MDE-MPCMs, which indicated that MDE and LAL–CAL have better chemical compatibility.

### 3.4 Moisture absorption/release properties evaluation

Fig. 5 shows the diagram of the moisture content for the samples at different times. 0–48 h represents the hygroscopic process under the condition of 100% RH, and 48–96 h displays the humidity release process of the samples in the environment of 11% RH. Fig. 5a shows the test process according to the method described in Section 2.3. In Fig. 5b, all calcined samples had a faster moisture absorption rate before 6 h, which will gradually slow down over time. The equilibrium moisture content was not reached at 48 h, and the moisture absorption trend still existed. The moisture release experiment was carried out immediately after the samples had been hygroscopic for 48 h. It can be seen that the moisture release rate of the samples was also faster at the beginning, but tended to balance over time. The humidity control performance of samples treated by

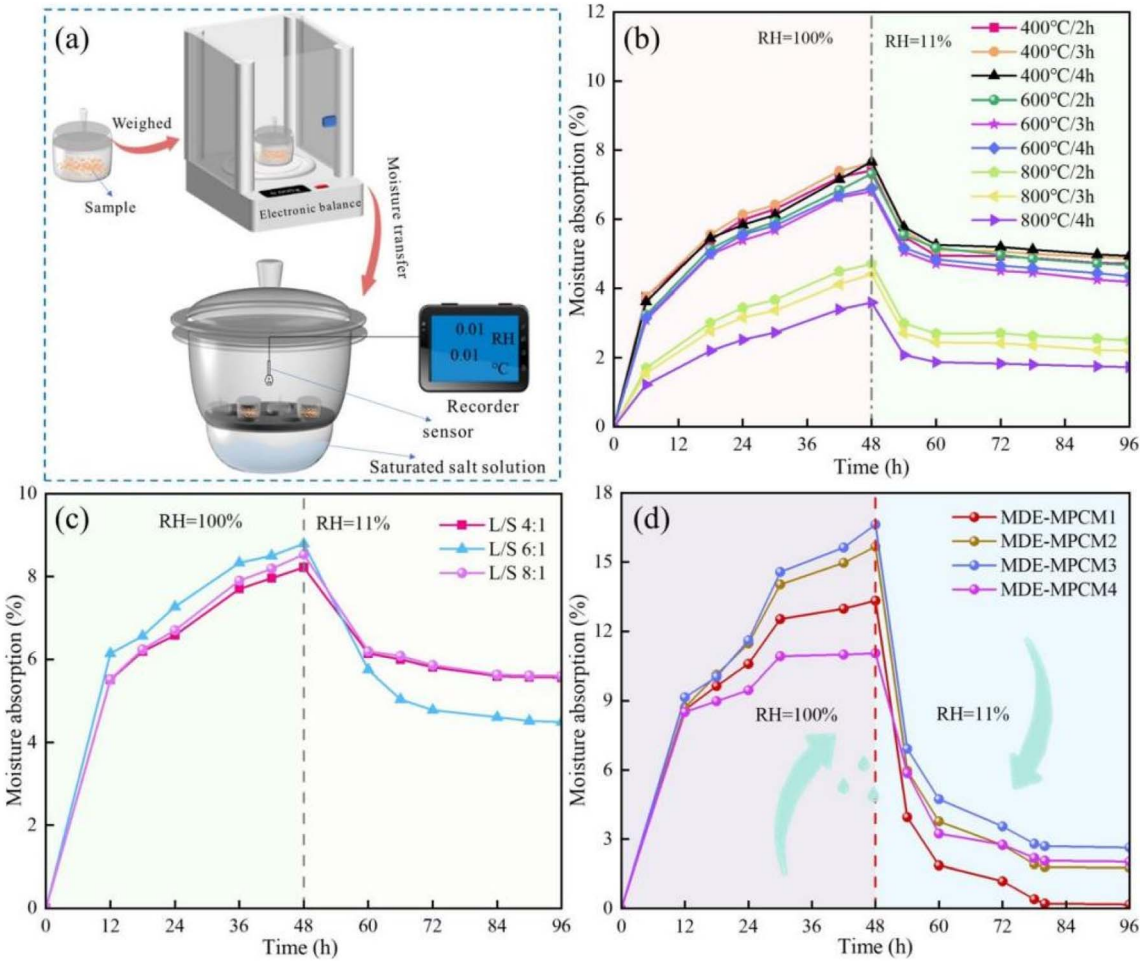


Fig. 5 Scheme of the experimental setup of (a) and the influence of different calcination conditions (b) and L/S ratio (c), (d) humidity control perfromance of the samples.

calcination at 400 °C per 3 h is optimal, with the maximum moisture absorption and release rates being 7.64% and 2.78%, respectively. Fig. 5c illustrates the moisture content relationship of the samples under optimal calcination conditions for further alkali treatment. The humidity regulation performance appeared to follow the trend of first increasing and then decreasing with the increase of L/S ratio, which may be because excessive alkali will destroy the internal pore structure of MDE and lead to the hygroscopic property of MDE was decreased. Compared with DE, the moisture absorption and release rate of MDE (L/S is 6 : 1) increased, which is perhaps because modification results in increasing the specific surface area and the porosity of MDE, thus improving the humidity control performance. Fig. 5d illustrates the effects of MDE content on the humidity control property of MDE-MPCMs. The moisture content of the samples changes rapidly in the first 12 h during the moisture absorption process of 0–48 h, and then increases slowly with the passage of time. The moisture absorption performance of the MDE-MPCMs increased first and then decreased with the increase of MDE content, and the moisture content reached the peak at 48 h when the MDE content was 15%. At this moment, the moisture absorption rate of MDE-MPCM3 is 16.63%, and the moisture absorption rates of MDE-MPCM1, MDE-MPCM2, and MDE-MPCM4 are 13.33%, 15.67% and 11.05% respectively. This may be because the humidity control ability is mainly affected by the hydrophilic –OH in the system when the low MDE content. With the increase of MDE, the specific surface area and the effective porosity of MDE-MPCMs were increased, thus the hygroscopic ability was enhanced. However, excessive MDE content will affect the formation of microcapsules, reduce the hydrophilic –OH content, cause gel agglomeration, block the pore structure, and reduce the hygroscopic and desorption properties. The moisture content of MDE-MPCMs also showed a similar change trend during the moisture release process of 48–96 h. When the MDE content is 15%, the moisture release rate of MDE-MPCM3 is the largest. Compared with other samples, MDE-MPCM3 has the best moisture control performance.

### 3.5 Phase change behaviors

Fig. 6 shows the phase change characteristics of PCMs and MDE-MPCMs. The encapsulation rate ($R$) and efficiency ($E$) of MDE-MPCMs were calculated from the formulas listed in reference,[53] and the relevant values are shown in Table 1. In Fig. 6a, the phase change temperatures of LAL and CAL were 22.45 and 49.02 °C, respectively. LAL had a solidification value, and CAL had two exothermic phenomena. For CAL, the liquid–solid phase change begins when the temperature drops to 47.55 °C, ends at 41.92 °C, and then the solid–solid phase transition begins. The latent heat of melting and solidification of LAL were 195.61 and 183.29 J $g^{-1}$, respectively, while the latent heat of melting of CAL was 234.59 J $g^{-1}$, and there were two peaks of heat release, 125.38 and 74.29 J $g^{-1}$, respectively. The phase change and solidification temperature of the LAL–CAL were 19.08 and 16.69 °C, and the latent heat of melting and solidification were 172.11 and 80.21 J $g^{-1}$, respectively. Simultaneously, there was one exothermic peak in the LAL–CAL eutectic curve, which showed that the mixing of LAL and CAL can eliminate the phenomenon of CAL multiple exothermic heat. In Fig. 6b, the microcapsules with different MDE content only show one peak during the heating and exothermic process, indicating that the phase change behaviors of MDE-MPCMs depend on the LAL–CAL. The phase change temperature and latent heat of MDE-MPCMs were lower than those of LAL–CAL, which was due to the heterogeneous nucleation between the core and shell material during encapsulation. The DSC value of MDE-MPCMs increased first and then decreased, and reached the maximum value (70.01 J $g^{-1}$) when MDE content was 15%. This may be because low MDE content will affect the formation of a continuous film and reduce the compactness. LAL–CAL will precipitate from the system during drying of the microcapsule, affecting the latent heat of the sample. As the MDE content increases, the interaction between MDE and the silicon shell prevents the leakage of LAL–CAL, thereby increasing the latent heat. However, when MDE content was 20%, the latent heat value of MDE-MPCM4 was significantly reduced, which may be because excessive MDE will cause LAL–CAL to leak out of the microcapsule, thus affecting the formation of MDE-MPCMs. To

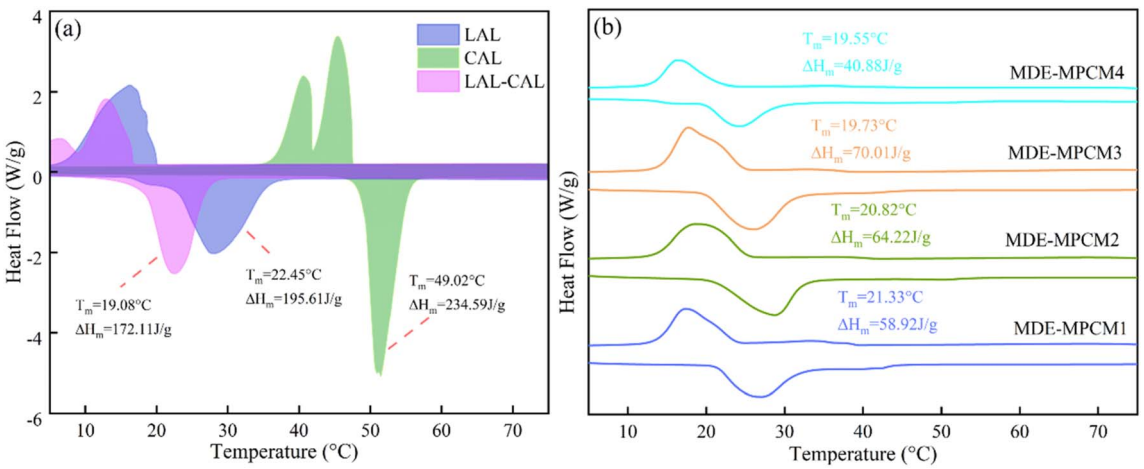


Fig. 6 The DSC curves of (a) LAL, CAL, and LAL–CAL; (b) MDE-MPCMs.

Table 1 Phase change parameters of the samples

| | Melting | | Solidifying | | | |
|---|---|---|---|---|---|---|
| Samples | Temperature (°C) | Latent heat (J g$^{-1}$) | Temperature (°C) | Latent heat (J g$^{-1}$) | *R* (%) | *E* (%) |
| LAL–CAL | 19.08 | 172.11 | 16.69 | 80.21 | — | — |
| MDE-MPCM1 | 21.33 | 58.92 | 24.10 | 58.10 | 34.2 | 46.4 |
| MDE-MPCM2 | 20.82 | 64.22 | 25.33 | 60.30 | 37.3 | 49.4 |
| MDE-MPCM3 | 19.73 | 70.01 | 24.87 | 66.35 | 40.7 | 54.0 |
| MDE-MPCM4 | 19.55 | 40.88 | 21.52 | 30.03 | 23.8 | 28.1 |

Table 2 Phase change parameters of the samples before and after the cycle

| Samples | Melting temperature (°C) | Latent heat (J g$^{-1}$) | *R* (%) |
|---|---|---|---|
| MDE-MPCM3 | 19.73 | 70.01 | 40.70 |
| MDE-MPCM3-50 | 19.70 | 68.71 | 39.92 |
| MDE-MPCM3-100 | 19.65 | 67.20 | 39.05 |

evaluate the long-term thermal reliability of MDE-MPCM3, the samples were subjected to 50 and 100 melting–freezing cycles. In Table 2, the MDE-MPCM3 exhibits excellent stability throughout the cycling test. The melting temperature remained basically unchanged, shifting from an initial 19.73 °C to 19.65 °C after 100 cycles. More importantly, the latent heat decreased from 70.01 J g$^{-1}$ to 67.2 J g$^{-1}$, with a loss of only 2.81 J g$^{-1}$. The result demonstrates that the material has better thermal reliability and thermal energy storage potential. In Table 3, compared with other microcapsules, MDE-MPCM3 prepared in this study has a suitable phase transition temperature and higher latent heat for the application of building energy conservation.

### 3.6 Temperature response capacity

The thermal regulation behaviors of microcapsules with 5–20% MDE content were investigated by infrared thermal imaging technology, and the surface temperature change images of MDE-MPCMs are shown in Fig. 7. All samples were designed as the same size cylinders and placed in a tin foil mold, which was heated or cooled on a thermostat. Fig. 7a shows the surface temperature image during the heating process. MDE-MPCMs presented similar temperatures within the first 10 s, and the value was about 19 °C. With the extension of heating time, the surface temperature of MDE-MPCMs changed continuously. As the heating time increases, the surface temperature of MDE-MPCMs continues to increase. At 60 s, the surface heating rate of MDE-MPCMs begins to be different, the sample morphology appears slightly different, and the surface is heated unevenly. After 100 s, the surface temperature of MDE-MPCMs continued to increase and formed a significant difference. Compared with other microcapsules, MDE-MPCM3 reached 120 s, which showed excellent heat storage performance and effectively suppressed the internal temperature fluctuation of the sample. The surface temperature of MDE-MPCM3 is about 28 °C at 120 s. The surface temperatures of MDE-MPCM1, MDE-MPCM2, and MDE-MPCM4 are aroundt 43 °C, 36 °C, and 45 °C, respectively. It may be because DE is inert and does not store latent heat, and the interaction between MPCM and DE is beneficial to enhance the heat storage capacity of materials. Meanwhile, it may be related to the content of heat storage materials encapsulated in microcapsules, and more LAL–CAL was conducive to the absorption of heat. In Fig. 7b, the surface temperature of MDE-MPCMs began to drop rapidly during the cooling process, but was almost unchanged for a period, which was caused by the heat release of the microcapsules. MDE-MPCM3 held heat for a longer time than other samples, further confirming that it stored more heat. Combined with the humidity control experiment, DSC test, and infrared thermal imaging analysis, results indicated that MDE-MPCM3 has better ability for humidity regulation and heat storage.

### 3.7 Thermal stability and leakage assessment

The TGA technology was used to characterize the thermal stability of MDE-MPCM3, as shown in Fig. 8. Both MDE and LAL–CAL had only one thermal decomposition stage, while MDE-MPCM3 had three thermal decomposition steps, indicating

Table 3 Comparison of thermal properties of MPCMs

| Samples | Melting temperature (°C) | Latent heat (J g$^{-1}$) | *R* (%) | Ref. |
|---|---|---|---|---|
| Capric-octadecanoic acid/vesuvianite | 26.90 | 14.10 | 9.6 | 54 |
| *N*-Octadecane/$SiO_2$ | 27.97 | 55.12 | 26.4 | 55 |
| Capric acid/$SiO_2$ | 32.01 | 61.16 | 38.0 | 56 |
| Lauric acid/$SiO_2$ | 37.50 | 41.80 | 21.7 | 57 |
| Methyl laurate/DE | 1.75 | 65.70 | 34.6 | 58 |
| MDE-MPCM3 | 19.73 | 70.01 | 40.7 | This paper |

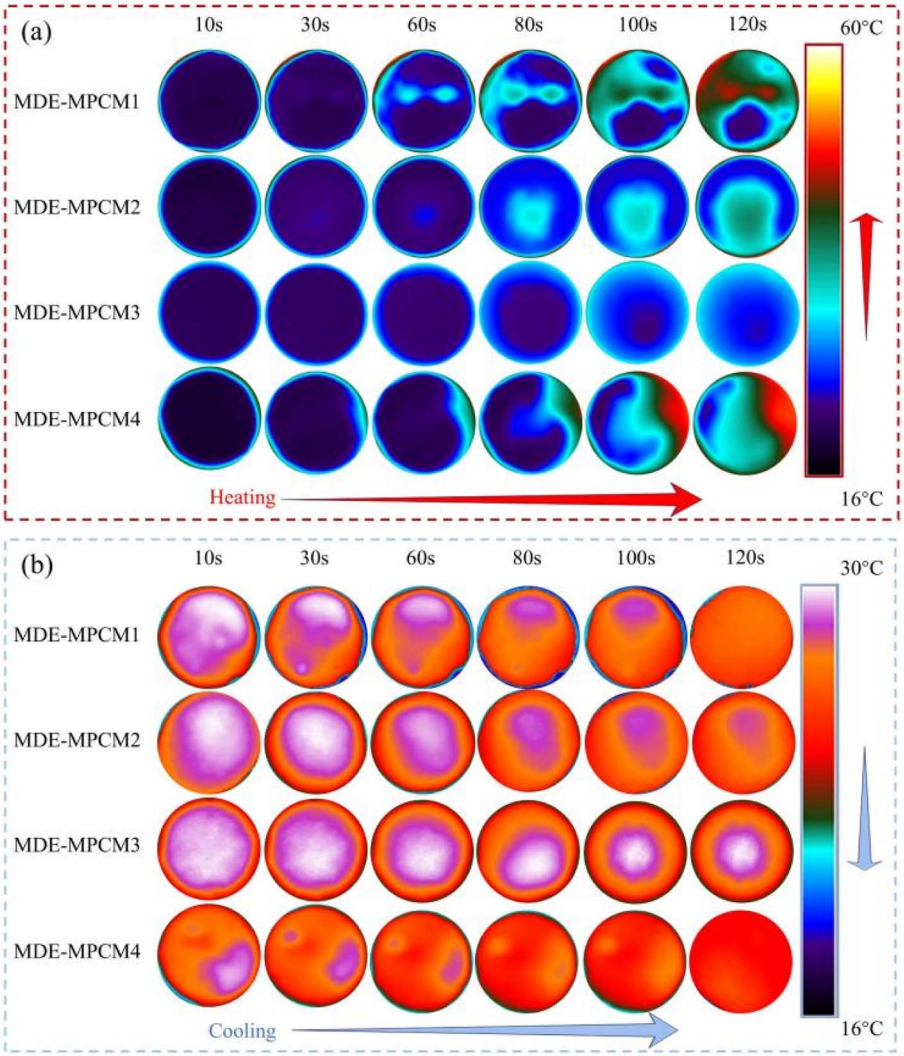


Fig. 7 The infrared thermographic images of MDE-MPCMs during (a) the heating and (b) cooling processes.

that the decomposition temperatures of LAL–CAL, silicon dioxide shell material, and MDE were different and immiscible. The mass loss of MDE was 7.66% at the beginning, which may be caused by the residual moisture. LAL–CAL appeared in a weightlessness zone of about 108 °C, reaching 202 °C, with almost complete weightlessness, which was perhaps caused by decomposition and volatilization. For MDE-MPCM3, the first partition curve at 115 °C was basically the same as LAL–CAL. The subsequent mass loss may be caused by further dehydration at high temperatures due to the presence of non-reactive –OH groups in the $SiO_2$. The addition of MDE delayed the weight loss temperature of LAL–CAL and had a good protective effect on it. Within the working range, the quality of MDE-MPCM3 does not change obviously, which confirms the excellent thermal stability of MDE-MPCM3 for building applications.

The leakage assessment was carried out to verify the morphological stability of MDE-MPCM3. Fig. 9 shows the leakage test process of MDE-MPCM3 heated to 50 °C. In 0–30 s, the appearance of LAL–CAL and MDE-MPCM3 remains

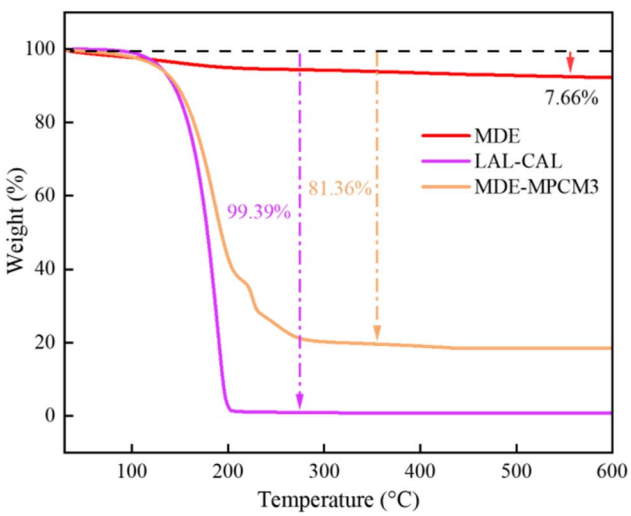


Fig. 8 The TGA curves of MDE-MPCM3.

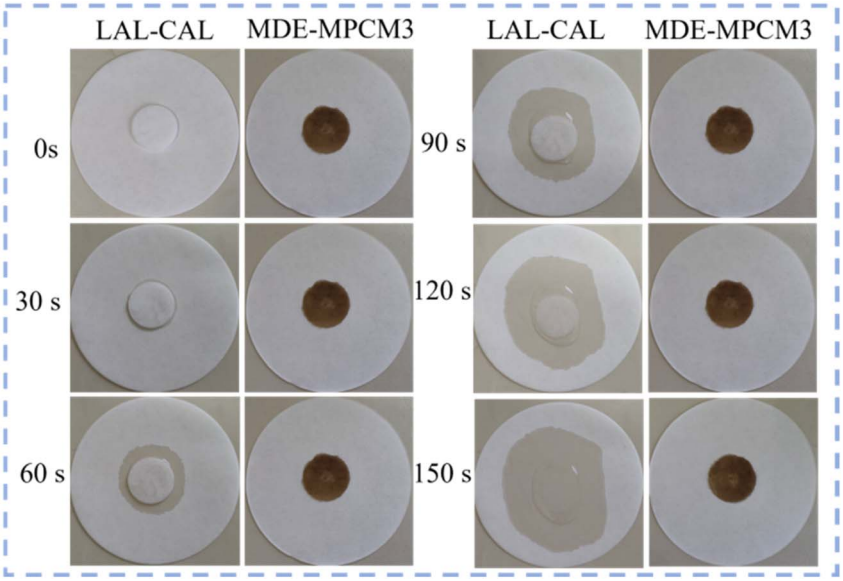


Fig. 9 The leakage photographs of LAL–CAL and MDE-MPCM3.

unchanged. At 60 s, LAL–CAL had a slight leakage, while MDE-MPCM3 had almost no change. The leakage traces of LAL–CAL gradually increased and showed a larger leakage area in 90–120 s, but MDE-MPCM3 still had no leakage sign. Reaching 150 s, LAL–CAL completely leaked, while MDE-MPCM3 had almost no leakage and presented better integrity. The results proved that MDE-MPCM3 had better morphological stability than LAL–CAL, which can be conducive to the application of humidity regulation and heat storage in buildings.

### 3.8 Micromorphology interpretation

The surface morphologies of DE, MDE, and MDE-MPCM3 were shown in Fig. 10. As can be seen from Fig. 10a and b, raw DE was disk-shaped, had impurities attached to the surface, and part pores were blocked, which was not conducive to the adsorption of water and the coating of phase change microcapsules. It means that raw DE was not suitable for direct use as the temperature and humidity control matrix. Fig. 10c shows the microscopic morphology of MDE, where part of the impurities attached to the surface of MDE were removed, and the pore structure channels were dredged, presenting a fine and dense distribution. For MDE, the adsorption capacity of water was enhanced and provided more heat storage space, which laid the foundation for the preparation of MDE-MPCM3 with excellent temperature and humidity control performance. Fig. 10d shows the surface morphology of MDE-MPCM3, which presented a nearly spherical shape and rough surface, and the perforations of misaligned distribution were formed in microspheres. Further proving that MDE attached to

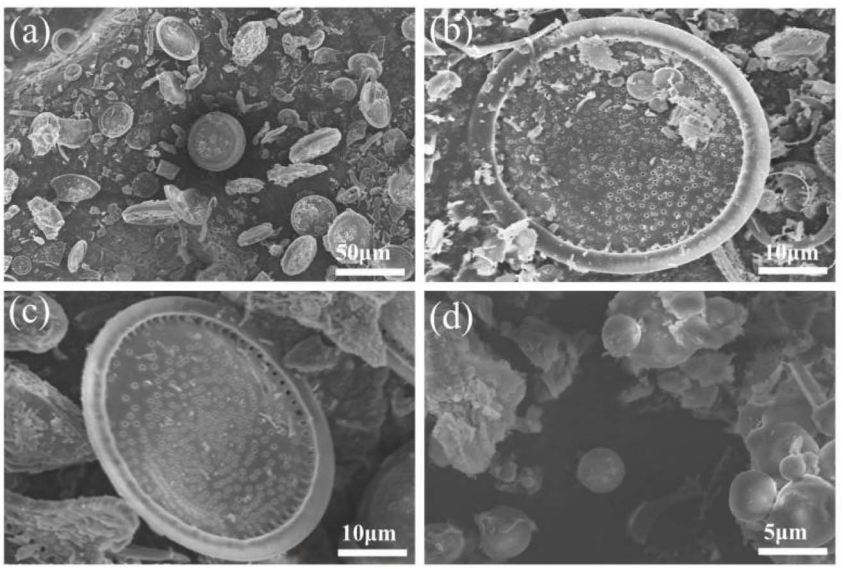


Fig. 10 The SEM of (a) and (b) DE, (c) MDE, and (d) MDE-MPCM3.

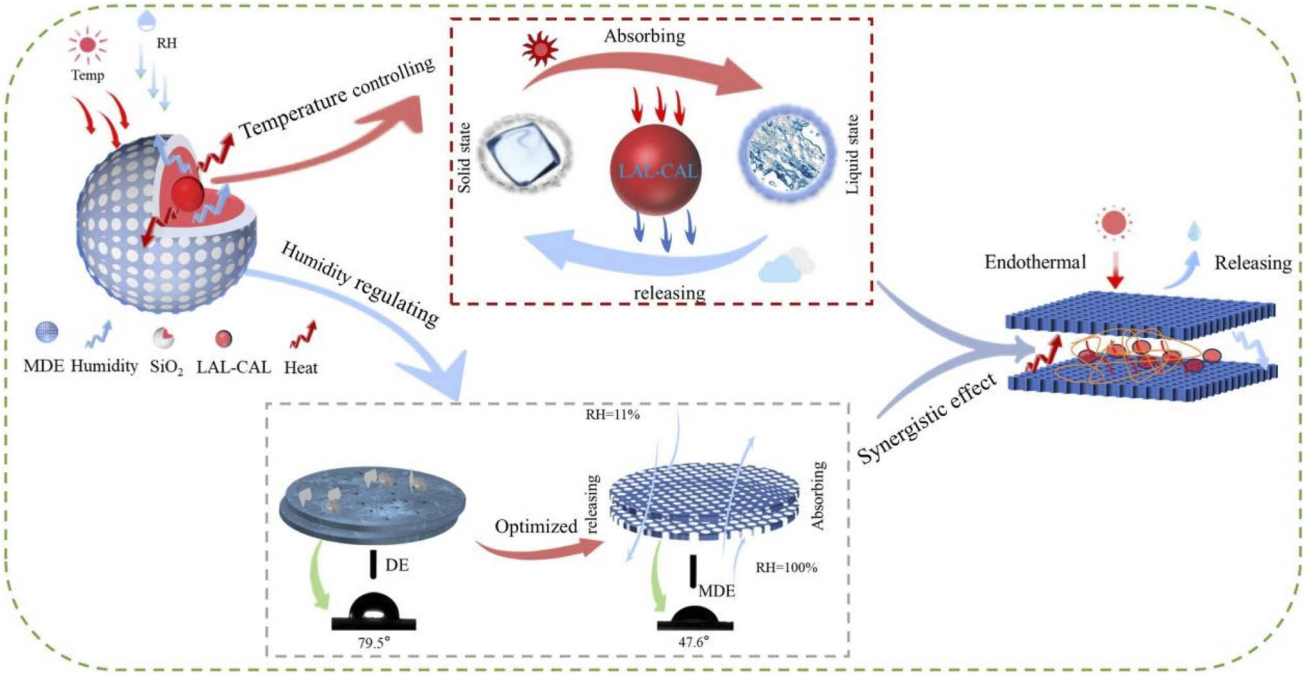


Fig. 11 The schematic diagram of the synergistic role of humidity-temperature control of MDE-MPCM3.

the surface plays a stable supporting role and successfully coats LAL–CAL to form the MDE-MPCM3.

### 3.9 Hygrothermal synergistic mechanism of MDE-MPCM3

The synergistic mechanism of humidity-temperature adjustment of MDE-MPCM3 is shown in Fig. 11. The water contact angles of DE and MDE were 79.5 and 47.6°, respectively, which shows typical hydrophilic behavior. The water contact angle was decreased, which can enhance the hydrophilicity of MDE. The surface impurities of MDE were reduced, and the pore structure channel of MDE was dredged, which indicated that loading MDE was beneficial to increase the area of heat transfer and moisture storage and strengthen the ability of temperature and humidity control of MDE-MPCM3. On the one hand, when the external temperature was higher than the phase transition temperature of LAL–CAL, it could absorb the external heat and reduce the external temperature. When the external temperature is lower than the phase transition temperature, LAL–CAL inside the MDE-MPCM3 releases internal heat and increases the outside temperature, thus inhibiting the fluctuation of the indoor environment temperature. On the other hand, because MDE has a larger specific surface area, fine and more porous distribution, it can realize the adsorption of water and achieve humidity regulation. When in the higher humidity environment, the humidity-regulating matrix of MDE can spontaneously absorb and store moisture content, and inhibit humidity change.

When the absolute indoor humidity is unchanged, the temperature rise will decrease the RH of the environment. At this time, LAL–CAL inside MDE-MPCM3 will absorb excess heat and increase the internal temperature, which will accelerate the evaporation of water and help MDE-MPCM3 to suppress indoor humidity fluctuations. The indoor RH was too high, MDE would absorb water vapor, and reduce the moisture content in the air, resulting in the ambient temperature being increased, and then LAL–CAL would absorb heat and delay the indoor temperature change. When MDE absorbs moisture, LAL–CAL will work and enhance the heat storage capacity of MDE-MPCM3, and after LAL–CAL absorbs heat will help MDE control the RH, which further indicates that there is a good synergistic effect among them. It shows that MDE-MPCM3 has great potential in the field of thermal energy storage and improving indoor comfort.

## 4 Conclusion

In this study, the new type of MDE-MPCMs was synthesized by MDE secondary encapsulation LAL–CAL with the sol–gel method for building energy conservation. The chemical compatibility between MDE and LAL–CAL in MDE-MPCMs was verified through FTIR analysis. Among the additive amounts of MDE from 5% to 20%, the MDE-MPCM3 (15%) exhibits better moisture regulation capacity and thermal storage performance. The maximum moisture absorption and release rates of MDE-MPCM3 can be reached at 16.63% and 13.99%, which have phase transition temperatures and latent heat of 19.73 °C and 70.01 J $g^{-1}$, respectively. It is worth noting that the synergistic mechanism of humidity regulation and heat storage of MDE-MPCM3 was revealed. When the MDE absorbs moisture, which will trigger the internal LAL–CAL to work, thereby exerting the heat storage capacity of MDE-MPCM3, while the heat absorption of LAL–CAL will help MDE control the change of indoor humidity. The MDE-MPCM3 can be used in thermal energy storage due to its excellent thermal properties and better humidity control performance.

## Conflicts of interest

There are no conflicts to declare.

## Data availability

The data supporting this article have been included as part of the supplementary information (SI). Supplementary information: one text, eleven figures, and three tables. See DOI: **https://doi.org/10.1039/d5ra07802d**.

## Acknowledgements

This work was supported by the Basic Research Projects in 2024 of the Department of Education of Liaoning Province, China (Grant numbers LJ212410148057) and Liaoning Key Lab of Petro-chemical Special Building Materials.

## References

1 X. Y. Li and R. M. Yao, *Energy Build.*, 2021, **235**, 110740.
2 D. H. Vu, K. S. Wang, B. H. Bac and B. X. Nam, *Constr. Build. Mater.*, 2013, **38**, 1066–1072.
3 P. Wolkoff, *Int. J. Hyg Environ. Health*, 2018, **221**, 376–390.
4 R. D. Ye, J. Wang, Y. N. Li, W. C. Sun, X. L. Zou, F. X. Wang and X. G. Shu, *Int. J. Energy Res.*, 2024, **2024**, 2859.
5 L. Brady and M. Abdellatif, *Energy Build.*, 2017, **149**, 142–150.
6 W. W. Che, C. Y. Tso, L. Sun, D. Y. K. Ip, H. Lee, C. Y. H. Chao and A. K. H. Lau, *Energy Build.*, 2019, **201**, 202–215.
7 E. Cuce, D. Harjunowibowo and P. M. Cuce, *Renew. Sustain. Energy Rev.*, 2016, **64**, 34–59.
8 Z. C. Xue, J. H. Wang, Y. Q. Diao and W. B. Hu, *Materials*, 2024, **17**(8), 1920.
9 P. Zhang, Y. Y. Cui, K. Q. Zhang, S. N. Wu, D. C. Chen and Y. F. Gao, *J. Clean. Prod.*, 2021, **279**, 123211.
10 D. K. Li, X. C. Zuo, X. Y. Zhang, Y. Tang, X. G. Zhao, Y. T. Zhang and H. M. Yang, *J. Energy Storage*, 2023, **68**, 107661.
11 P. Liu, X. B. Gu, L. Bian, L. H. Peng and H. C. He, *J. Therm. Anal. Calorim.*, 2019, **138**, 359–368.
12 X. C. Zuo, X. Y. Zhang, Y. L. Tang, Y. T. Zhang, X. Li and H. M. Yang, *Appl. Clay Sci.*, 2024, **247**, 107214.
13 D. Ding and M. H. Qin, *Appl. Therm. Eng.*, 2024, **257**, 124329.
14 X. Li and M. Y. Ran, *Materials*, 2023, **16**(15), 5211.
15 M. H. Qin, O. S. Rasmussen, J. Chen and L. Wadso, *Build. Environ.*, 2024, **261**, 111757.
16 X. Q. He, H. B. Zhang, L. Qiu, Z. D. Mao and C. N. Shi, *Energy Build.*, 2021, **236**, 711092.
17 C. C. Li, M. F. Wang, B. S. Xie and Y. L. He, *Renewable Energy*, 2024, **229**, 120731.
18 S. Y. Liu, W. Gao, J. Deng, M. Q. Wang, M. Zhou and H. Y. Liang, *J. Energy Storage*, 2024, **99**, 113315.
19 A. Hassan, A. Wahab, M. A. Qasim, M. M. Janjua, M. A. Ali, H. M. Ali, T. R. Jadoon, E. Ali, A. Raza and N. Javaid, *Renewable Energy*, 2020, **145**, 282–293.
20 Y. H. Li, X. Zhao, Y. L. Tang, X. C. Zuo and H. M. Yang, *Adv. Funct. Mater.*, 2024, **34**(39), 2403059.
21 M. Q. Wang, S. Y. Liu, W. Gao and M. Zhou, *J. Energy Storage*, 2024, **78**, 110091.
22 X. G. Zhao, Y. L. Tang, X. Y. Zhang, X. C. Zuo and H. M. Yang, *Appl. Clay Sci.*, 2022, **229**, 106678.
23 B. Nghana and F. Tariku, *Build. Environ.*, 2016, **99**, 221–238.
24 M. J. Song, F. X. Niu, N. Mao, Y. X. Hu and S. M. Deng, *Energy Build.*, 2018, **158**, 776–793.
25 B. M. Wang, M. Shi, H. Yao, X. Yang, S. Guo, Y. Liu, Q. X. Hua, B. Shen, P. F. Liu and J. W. Tang, *Energy Build.*, 2023, **279**, 112706.
26 J. Jin, L. Liu, R. H. Liu, H. Wei, G. P. Qian, J. L. Zheng, W. Xie, F. P. Lin and J. Xie, *Constr. Build. Mater.*, 2019, **226**, 616–624.
27 S. Y. Liu, J. Han, L. N. Wang, Y. Gao, H. Sun and W. L. Li, *RSC Adv.*, 2020, **10**, 25864–25873.
28 N. Philip, G. R. Dheep and A. Sreekumar, *J. Energy Storage*, 2020, **27**, 1016060.
29 M. Q. Wang, S. Y. Liu, J. Han, R. X. Bai, W. Gao and M. Zhou, *Sol. Energy*, 2024, **273**, 112501.
30 J. J. Cheng, M. Y. Kang, W. Lin, C. C. Liang, Y. Q. Liu, Y. P. Wang, S. S. Niu and F. Zhang, *Constr. Build. Mater.*, 2023, **362**, 129764.
31 M. Ghufran and D. Huitink, *J. Mater. Sci.*, 2023, **58**, 7673–7689.
32 C. Q. Zhu, Y. X. Lin and G. Y. Fang, *Appl. Therm. Eng.*, 2020, **169**, 114943.
33 J. Zhao, Y. Y. Yang, Y. Li, L. Zhao, H. Wang, G. L. Song and G. Y. Tang, *Sol. Energy Mater. Sol. Cell.*, 2017, **168**, 62–68.
34 S. Yuan, R. Yan, B. Ren, Z. Du, X. Cheng, X. Du and H. Wang, *Renewable Energy*, 2021, **180**, 725–733.
35 X. Z. Wang, W. Y. Gao, S. Yan, M. H. Niu, G. Liu and H. S. Hao, *Constr. Build. Mater.*, 2018, **175**, 187–195.
36 B. Zhou, J. Shi and Z. Q. Chen, *Appl. Therm. Eng.*, 2018, **128**, 604–613.
37 X. G. Wang, Y. X. Lei, Z. F. Chen and W. y. Lei, *J. Colloid Interface Sci.*, 2021, **595**, 25–34.
38 J. H. Park, Y. U. Kim, J. Jeon, B. Y. Yun, Y. Kang and S. Kim, *Sci. Total Environ.*, 2021, **775**, 145552.
39 Y. Fraine, C. Seladji and A. Ait-Mokhtar, *Build. Environ.*, 2019, **154**, 145–154.
40 Z. B. Hu, S. L. Zheng, Z. M. Sun, Y. Chen and Y. Yan, *Sci. Technol. Built Environ.*, 2017, **23**, 1305–1313.
41 Y. Konuklu, O. Ersoy and O. Gokce, *Appl. Therm. Eng.*, 2015, **91**, 759–766.
42 J. Y. Zheng, J. Shi, Q. Ma, X. Dai and Z. Q. Chen, *Appl. Therm. Eng.*, 2017, **114**, 450–456.
43 J. Fort, J. Kocí, J. Pokorny, L. Podolka, M. Kraus and R. Cerny, *Appl. Sci.*, 2020, **10**(24), 9116.
44 Z. D. Mao, H. B. Zhang, Y. Li, X. X. Wang, Q. Wei and J. C. Xie, *J. Build. Eng.*, 2021, **43**, 103122.
45 Z. B. Hu, S. L. Zheng, M. Z. Jia, X. B. Dong and Z. M. Sun, *Adv. Powder Technol.*, 2017, **28**, 1372–1381.
46 C. C. Li, M. Wang, B. S. Xie, H. Ma and J. Chen, *Renewable Energy*, 2020, **147**, 265–274.
47 G. L. Zhang, D. Q. Cai, M. Wang, C. L. Zhang, J. Zhang and Z. Y. Wu, *Microporous Mesoporous Mater.*, 2013, **165**, 106–112.

48 M. J. Abden, Z. Tao, Z. Pan, L. George and R. Wuhrer, *Appl. Energy*, 2020, **259**, 114113.
49 N. Zhu, X. K. Li, P. F. Hu, F. Lei, S. Wei and W. T. Wang, *Energy*, 2022, **239**, 122433.
50 H. Yang, Y. Liu, X. F. Kong, W. H. Chen and C. Q. Yao, *J. Cent. South Univ.*, 2018, **25**, 2387–2398.
51 Y. Y. Yang, Z. H. Shen, W. D. Wu, H. Zhang, Y. Ren and Q. G. Yang, *Build. Environ.*, 2022, **226**, 109732.
52 D. D. Xu, Y. Huang, W. W. Liu, T. Sun and M. J. Zhang, *Constr. Build. Mater.*, 2023, **378**, 131068.
53 J. K. Ma, H. Liu, D. W. Sun and S. P. Cui, *Constr. Build. Mater.*, 2024, **413**, 134831.
54 Z. Chen and M. H. Qin, *Appl. Therm. Eng.*, 2016, **98**, 1150–1157.
55 F. He, X. D. Wang and D. Z. Wu, *Energy*, 2014, **67**, 223–233.
56 F. Meng, L. Dong, Y. L. Wu, X. Shu, Y. D. Guo and Q. P. Ran, *Constr. Build. Mater.*, 2023, **404**, 133208.
57 H. M. Yuan, H. Bai, X. Zhang, J. Zhang, Z. F. Zhang and L. Yang, *Sol. Energy Mater. Sol. Cell.*, 2019, **191**, 243–257.
58 Z. Y. Liu, J. Y. Jiang, X. Jin, Y. C. Wang and Y. S. Zhang, *J. Energy Storage*, 2023, **68**, 107665.